Chemical Science

ROYAL SOCIETY OF CHEMISTRY

EDGE ARTICLE

View Article Online
View Journal | View Issue

Cite this: *Chem. Sci.*, 2023, **14**, 12182

All publication charges for this article have been paid for by the Royal Society of Chemistry

Received 31st July 2023
Accepted 30th September 2023

DOI: 10.1039/d3sc03972b

rsc.li/chemical-science

A collagen-immobilized nanodevice for *in situ* ratiometric imaging of cancer biomarkers in the tumor microenvironment†

Fengyu Tian, Shurui Zhou, Shiyi Xie, Zhenhua Zhang, Ling Peng, Ling Jiang, Zeyuan Wang, Zhou Nie and Yan Huang *

Monitoring the spatiotemporal dynamics of cancer biomarkers within the tumor microenvironment (TME) is critical to understanding their roles in tumorigenesis. Here, we reported a multifunctional fusion protein (collagen-binding domain and duck circovirus tag fused to mCherry, CBD-mCherry-DCV) capable of binding collagen with high affinity and covalently binding specific nucleic acids with exceptional efficiency. We then constructed a chimeric protein–nucleic acid nanodevice (**CPNN**) using CBD-mCherry-DCV and an aptamer-based sensing module to enable spatially controlled ratiometric imaging of cancer biomarkers in the TME. The collagen-anchoring module CBD-mCherry-DCV allowed specific immobilization of **CPNN** on 3D multicellular tumor spheroids, enabling the sensing module to achieve "off–on" fluorescence imaging of cancer biomarkers upon specific target recognition by an aptamer. Taking advantage of the constant fluorescence signal of mCherry and the activatable fluorescence response of Cy5 to specific cancer biomarkers, the detection sensitivity and reliability of **CPNN** were improved by self-calibrating the signal intensity. Specifically, **CPNN** enabled ratiometric fluorescence imaging of varying concentrations of exogenous PDGF-BB and ATP in tumor spheroids with a high signal-to-background ratio. Furthermore, it allowed the visual monitoring of endogenous PDGF-BB and ATP released from cells. Overall, this study demonstrates the potential of the nanodevice as a versatile approach for the visualization and imaging of cancer biomarkers in the TME.

Introduction

The tumor microenvironment (TME) is a highly complex physical and biochemical system.[1,2] Due to their critical role in regulating cellular metabolism and intercellular communication, the dysregulated expression of various biomolecules in the TME is closely associated with tumor growth, invasion, and metastasis, making them valuable cancer biomarkers.[3,4] However, tracking cancer biomarkers in the TME with high temporal and spatial resolution remains challenging for conventional assays, including flow cytometry, enzyme-linked immunosorbent assay, immunostaining, and mass spectrometry.[5–7] Therefore, *in situ* imaging of cancer biomarkers with high resolution in the TME is urgently needed to study their functions in cancer biology and to facilitate early cancer diagnosis and treatment.

The development of functional DNA-based cell surface sensors has opened new possibilities for *in situ* imaging of cancer biomarkers in the TME.[8–13] Benefiting from the exceptional programmability and flexibility of functional DNA, these sensors enable the detection of various relevant information in the TME with high spatial resolution, including extracellular pH,[14,15] metal ions,[16] small molecules,[17] and gaseous molecules.[18,19] Despite remarkable progress, current approaches for cell surface localization imaging and biosensing within the TME typically depend on lipid-based membrane modification or chemical modification for cell surface engineering. Consequently, they suffer from a lack of cell selectivity, cellular internalization of signal probes, and interference with the biological function of membrane proteins.[20–24] Furthermore, these conventional approaches generally rely on the absolute intensity-dependent signal readout, which can be influenced by various analyte-independent factors, leading to inaccurate sensing and imaging results.[25] In contrast, ratiometric measurements can minimize nonspecific effects by self-calibrating the signal intensity, thereby increasing the sensitivity and reliability of detection.[26–28] Nevertheless, developing a ratiometric fluorescent reporter for real-time monitoring and *in situ* imaging of cancer biomarkers in the

State Key Laboratory of Chemo/Biosensing and Chemometrics, College of Chemistry and Chemical Engineering, Hunan Provincial Key Laboratory of Biomacromolecular Chemical Biology, Hunan University, Changsha, 410082, P. R. China. E-mail: yanhuang@hnu.edu.cn

† Electronic supplementary information (ESI) available. See DOI: https://doi.org/10.1039/d3sc03972b

TME remains a significant challenge due to the lack of molecular targeting tools with high affinity, stability, and versatility in the TME.

Collagen, an extracellular matrix protein, has recently emerged as a promising target in the TME due to its overexpression in various cancers.[29–31] Under normal physiological conditions, collagen is insoluble and cannot penetrate most tissues due to the limited permeability of the vascular system. Conversely, in the TME, collagen becomes abnormally exposed to the bloodstream due to the hyperpermeability of the tumor vasculature.[32,33] Based on this, Hubbell's group developed a series of simple engineered collagen-binding immunotherapies to improve safety and antitumor efficacy by utilizing the A3 collagen-binding domain (CBD) of von Willebrand factor (VWF) with a high affinity for collagen.[34,35] Accordingly, a nanodevice using a collagen binding strategy shows significant potential for *in situ* imaging of biomarkers within the TME, while no related work has been reported.

Thus motivated, here we reported a novel multifunctional fusion protein CBD-mCherry-DCV (CmD) by genetic engineering and then constructed a chimeric protein-nucleic acid nanodevice (**CPNN**) for *in situ* ratiometric imaging of cancer biomarkers in the TME (Scheme 1). The proposed CmD consists of three functional units: (1) CBD as an anchoring element for binding collagen in the TME, (2) the HUH-endonuclease domain (duck circovirus, DCV) as a linking element for covalent coupling of protein and DNA, and (3) mCherry as an internal reference element for self-calibration.[36,37] By employing DCV as a linker, we covalently conjugated the multifunctional CmD to the aptamer-designed DNA sensing module, thus conferring target recognition and signal-read-out capacity to **CPNN**. **CPNN** presented an "always on" reference fluorescence signal and an "activatable" fluorescence signal in response to cancer biomarkers. Subsequently, **CPNN** was able to efficiently bind collagen in the TME for *in situ* ratiometric imaging of cancer biomarkers. As a proof of concept, we selected PDGF-BB, one of the major pro-angiogenic factors induced by the necrotic and hypoxic TME in various malignancies, as an example.[38,39] We demonstrated that the PDGF-BB-triggered **CPNN ($CPNN_{PDGF}$)** enabled visual monitoring of varying concentrations of exogenous PDGF-BB and endogenous PDGF-BB released from cells in tumor spheroids. High accuracy and sensitivity were achieved by benefiting from the colocalization of the nanodevice and the target molecule and the self-calibration of the ratiometric signal. Significantly, replacing the aptamer with others can expand the nanodevice to be a promising platform for detecting different tumor-associated markers in the TME. An ATP-responsive **CPNN ($CPNN_{ATP}$)** enabling ratiometric fluorescence imaging of ATP in tumor spheroids with a high signal-to-background ratio was fabricated. Moreover, unlike localization on the cell surface, **CPNN** binding to collagen prevented internalization into cells and kept it in the TME for efficient detection.[40] Therefore, this method provides an effective tool for the in-depth study and *in situ* imaging of cancer biomarkers in the TME.

Results and discussion

Preparation and characterization of the fusion protein CmD

The multifunctional fusion protein CBD-mCherry-DCV (CmD) was designed and biosynthesized using the *E. coli* expression system. The structural details of CmD are described in Fig. S1 and S2.† This fusion protein contained a CBD domain with a high affinity for collagen,[33] a fluorescent protein domain for self-calibration, and a HUH-endonuclease domain (DCV) for efficient protein–DNA covalent binding.[41] Among these, the fluorescent protein domain can be flexibly designed according to experimental requirements, and mCherry was chosen in this study due to its low intracellular background during cell imaging. In addition, glycine–serine (GlySer) linkers are introduced between different domains in the fusion protein to minimize inter-domain interactions.[42]

The molecular weight and optical properties of the obtained fusion proteins CmD and mCherry-DCV (mD, used as a control protein) were analyzed by SDS-polyacrylamide gel electrophoresis (SDS-PAGE) and fluorescence spectroscopy. As expected, CmD was of high purity with a molecular weight of approximately 65 kDa, and the control protein mD had a molecular weight of approximately 46 kDa (Fig. S3†), which agreed with the calculated theoretical protein sizes. Both CmD and mD exhibited the same excitation (580 nm) and emission (610 nm) wavelengths as mCherry, suggesting the minimal influence of the N- and C-terminal connexins on the fluorescence properties of mCherry (Fig. 1A and S4†). The stability of CmD in different physiological environments was further studied. Fig. 1B demonstrates that the fluorescence intensity of CmD remained constant over a range of pH values (4–9). This pH stability can be attributed to the distinctive barrel shape of mCherry, which protects the chromophore.[43] Furthermore, CmD maintained a steady fluorescence intensity over a week in different simulated physiological or pathological pH, such as pH 5.0 for lysosomes, pH 6.5 for the TME, and pH 7.4 for the normal tissues (Fig. 1C). CmD exhibited excellent fluorescence stability over a wide pH range and for prolonged periods of time, providing a significant advantage in tumor imaging applications.

By incorporating the CBD and DCV domains, CmD exhibited remarkable bispecificity, enabling it to bind collagen in the TME and link to nucleic acids covalently. The bispecificity of the obtained CmD was investigated by SDS-PAGE and fluorescence imaging. Gel shift analysis demonstrated that when incubated with a single-stranded DNA containing the DCV-specific recognition sequence ($ssDNA_{DCV}$), both CmD and mD formed a covalent adduct (CmD-$ssDNA_{DCV}$) with $ssDNA_{DCV}$ in the presence of Mn^{2+}, respectively (Fig. 1D). In addition, good conjugation was achieved with a 1 : 1 ratio of the fusion protein to $ssDNA_{DCV}$, consistent with the results reported in the literature.[36] The conjugation reaction is rapid and efficient, resembling click chemistry-like biochemical reactions under physiological conditions, and has the potential for versatile one-pot labeling.[41] Notably, due to the stable covalent bond between DCV and $ssDNA_{DCV}$, CmD-$ssDNA_{DCV}$ showed satisfactory

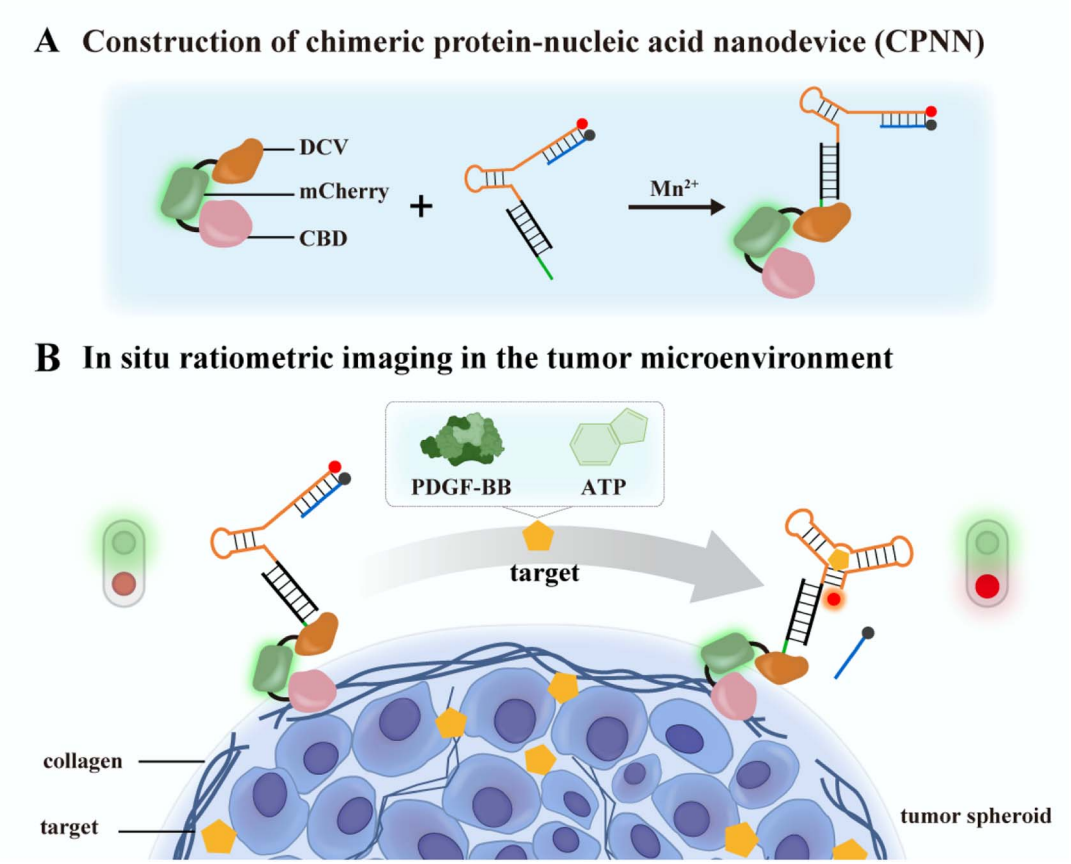

Scheme 1 Schematic showing the working principle of a collagen-immobilized nanodevice for *in situ* fluorescence imaging of cancer biomarkers in the TME.

stability (Fig. S5†). This stability is a foundation for future sensing and imaging applications. The collagen-dependent anchoring performance of CmD was then evaluated on the collagen-coated or the collagen-free 96-microwell plate. A clear change in the mCherry signal was observed in the collagen-coated wells after incubation with CmD for 30 min, followed by a gradual increase in the fluorescence signal with prolonged incubation (Fig. S6 and S7,† pseudo green). In contrast, the collagen-free well showed a negligible signal (Fig. S6†). Moreover, both collagen-coated and collagen-free wells showed minimal fluorescence after MD treatment (Fig. 1E, F and S6†), confirming that the observed fluorescence resulted from CBD-mediated anchoring. Importantly, CmD demonstrated stable anchoring on collagen for at least 4 hours under our experimental conditions (Fig. S8†). To illustrate the bispecificity of CmD more intuitively, we prepared the covalent adducts (CmD-ssDNA$_{DCV}$-Cy5 and mD-ssDNA$_{DCV}$-Cy5) by conjugating a Cy5-labeled ssDNA$_{DCV}$ (ssDNA$_{DCV}$-Cy5) to the fusion proteins. Subsequently, the adducts were incubated in the collagen-coated wells and subjected to fluorescence imaging, respectively. Fig. 1E and F illustrate that the collagen-coated well incubated with CmD-ssDNA$_{DCV}$-Cy5 exhibited bright fluorescence in the mCherry and Cy5 (pseudo red) channels. Notably, these two signals presented a positive correlation with incubation time and showed a significant colocalization with a Pearson's correlation coefficient (PC) of 0.81 (Fig. 1E and S9†). Conversely, the control well treated with mD-ssDNA$_{DCV}$-Cy5 did not exhibit discernible mCherry or Cy5 signals. These results confirmed that the fusion protein CmD possesses the functions we designed, including high-affinity binding to collagen and efficient conjugation to single-stranded DNA. As a dual high-affinity "bridge" protein, CmD opens new possibilities for *in situ* imaging of targets in the TME.

CPNN$_{PDGF}$-based PDGF-BB sensing in solution

Tumor cells often secrete various growth factors and cytokines as signalling molecules to influence host cells, predominantly promoting tumor growth and metastasis.[38] Notably, PDGF-BB and PDGFR-β are integral components of the ligand tyrosine kinase receptor system, critically involved in angiogenesis and blood vessel formation.[39,44] PDGF-BB plays a critical role in establishing an immunosuppressive TME.[45,46] Here, we first developed a PDGF-BB-responsive **CPNN** as a proof of concept. A sensing module (S_{PDGF}) was designed based on the structural switching of the aptamer of PDGF-BB. S_{PDGF} comprises three partially complementary strands, a FAM-labeled PDGF-BB aptamer strand (Apt-FAM), a quencher-modified strand (cDNA-BHQ1) that can complement the 5′ terminal sequence of Apt-FAM, and a DCV-specific recognition sequence-containing

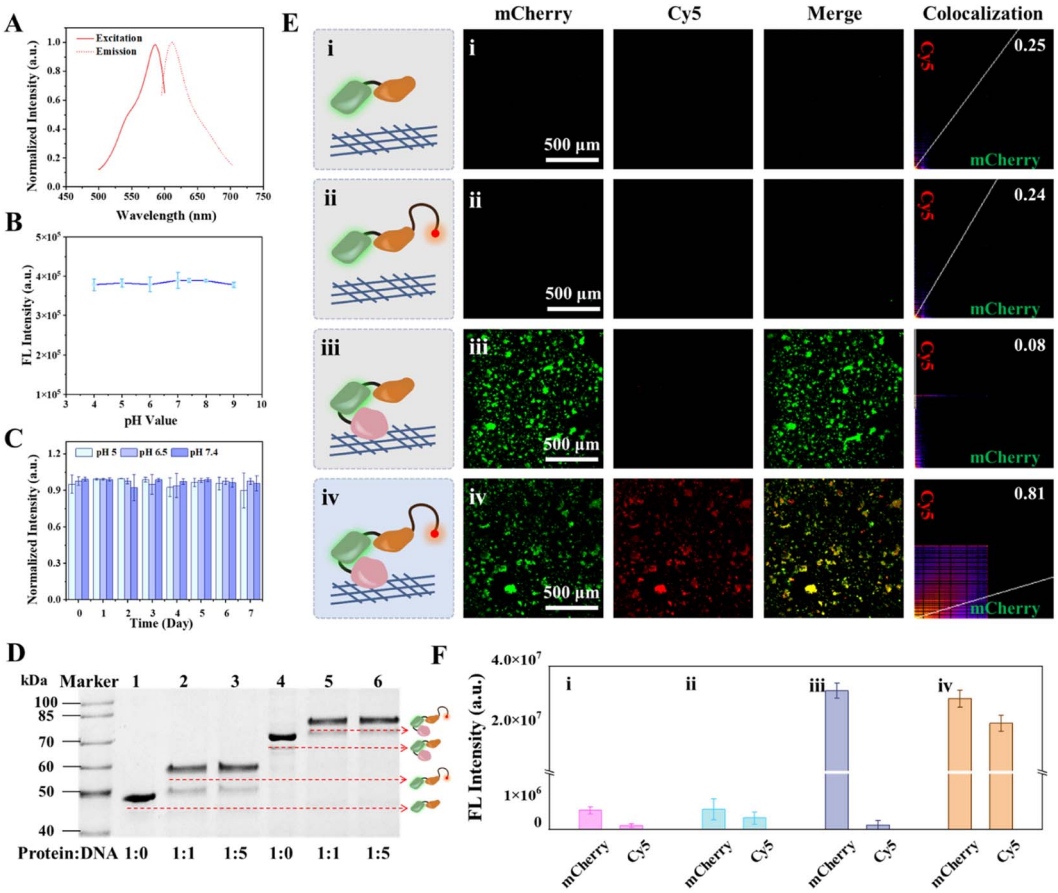

Fig. 1 Preparation and characterization of the engineered fusion protein CmD. (A) Fluorescence emission and excitation spectra of CmD. (B) Fluorescence emission stability of CmD at different pH values. (C) Time-dependent fluorescence intensity of CmD at pH 5.0, 6.5, and 7.4 over 7 days. (D) SDS-PAGE analysis of the chimeric protein–nucleic acid conjugate formation by the fusion protein (CmD or mD) and $ssDNA_{DCV}$ in HUH buffer. (E) Fluorescence images and (F) corresponding fluorescence intensity of CmD or mD incubated with collagen in the presence or absence of $ssDNA_{DCV}$-Cy5. (i) Collagen III + mD; (ii) collagen III + mD + $ssDNA_{DCV}$-Cy5; (iii) collagen III + CmD; (iv) collagen III + CmD + $ssDNA_{DCV}$-Cy5. Collagen III, 10 μg mL; CmD, 1 μM; $ssDNA_{DCV}$-Cy5, 1 μM. mCherry: excitation wavelength (E_x) 555 nm/emission wavelength (E_m) 610 nm; Cy5: E_x 635 nm/E_m 670 nm. Scale bar, 500 μm.

strand ($cDNA_{DCV}$) that can complete the 3′ terminal sequence of Apt-FAM (Fig. S10†). After S_{PDGF} was prepared through hybridization, it was covalently bound to CmD to obtain $\mathbf{CPNN}_{PDGF}$ (Scheme 1).

The capability of the proposed S_{PDGF} to detect PDGF-BB in the buffer was first investigated (Fig. 2A). As expected, S_{PDGF} exhibited a low fluorescent background in the buffer (Fig. 2B), suggesting the successful assembly and the efficient Förster resonance energy transfer between FAM and the quencher. In the presence of PDGF-BB, there was an approximately 6.9-fold increase in fluorescence intensity, which indicated that the specific binding of PDGF-BB to its aptamer led to the release of cDNA-BHQ1 and fluorescence recovery. Some specific nucleotides in the aptamer sequence were mutated (mApt-FAM) to generate mS_{PDGF} as a control. For mS_{PDGF}, no obvious increase in fluorescence intensity was detected before and after the addition of PDGF-BB, thereby confirming the essential role of the aptamer sequence in the sensing module. In addition, the fluorescence characteristics of S_{PDGF} were further explored by quantifying its relative fluorescence quantum yield (Φ) both before and after incubation with PDGF-BB. As shown in Table S5,† the relative fluorescence quantum yield of S_{PDGF} was significantly increased after incubation with PDGF-BB. These data demonstrated the capability of S_{PDGF} to detect PDGF-BB with high sensitivity and selectivity.

After optimizing the S_{PDGF} sequence, concentration, and buffer (Fig. S11–S13†), we further evaluated the analytical performance of S_{PDGF} for PDGF-BB detection. Real-time fluorescence analysis showed that the fluorescence intensity of the PDGF-BB-treated S_{PDGF} increased continuously with incubation time, reaching an almost plateau level within approximately 60 min (Fig. 2C). As depicted in Fig. 2D, the fluorescence signal increased with increasing PDGF-BB concentrations. It exhibited a linear relationship in the concentration range of 0.2–12 nM with a detection limit of 0.1 nM (3σ/slope, Fig. 2E). It is noteworthy that the designed S_{PDGF} can detect PDGF-BB levels ranging from several hundred pM to low nM levels, which is in good agreement with the concentration of PDGF-BB observed in serum (0.4–0.7 nM under physiological conditions and higher under pathological conditions such as tumors).[47,48]

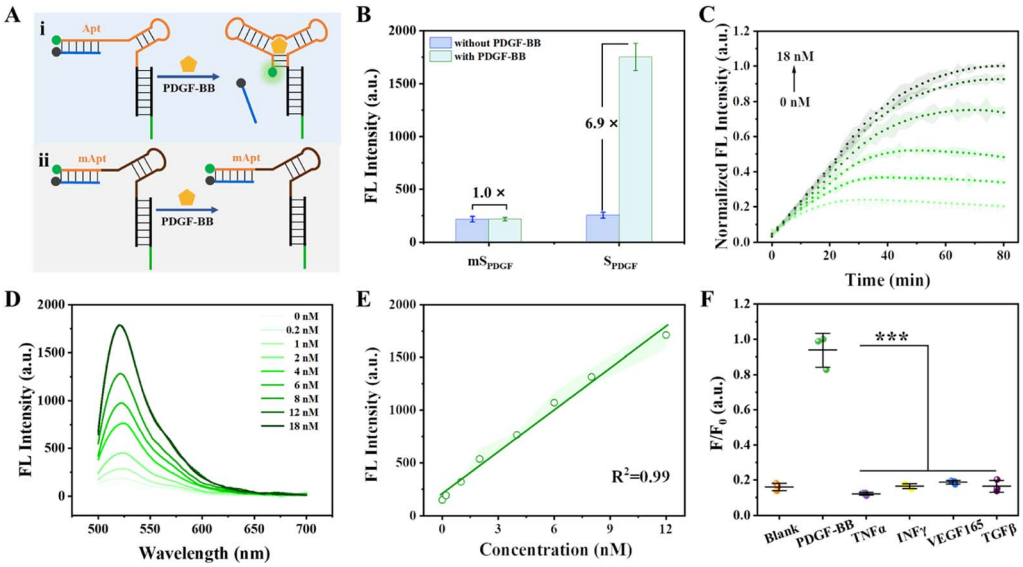

Fig. 2 Evaluation of S_{PDGF} for PDGF-BB detection in the buffer. (A) Schematic illustration of S_{PDGF} and mS_{PDGF} in response to PDGF-BB. (B) Fluorescence intensity of mS_{PDGF} and S_{PDGF} treated with or without PDGF-BB. (C) Fluorescence kinetics of S_{PDGF} treated with different concentrations of PDGF-BB. (D) Fluorescence spectra and (E) linear response of S_{PDGF} responding to varying concentrations of PDGF-BB. (F) The specificity of S_{PDGF} against other proteins. S_{PDGF}, 20 nM; each cytokine, 100 nM.

Furthermore, only PDGF-BB can increase the fluorescence intensity of S_{PDGF} compared to other cytokines, indicating the high selectivity of S_{PDGF} towards PDGF-BB (Fig. 2F).

The excellent sensing performance of S_{PDGF} encouraged us to investigate the viability of **CPNN$_{PDGF}$** as a ratiometric sensing probe for PDGF-BB monitoring. As shown in Fig. S14A,† **CPNN$_{PDGF}$** consisted of a CmD-based localization module and a S_{PDGF}-based sensing module. Specifically, the FAM signal in S_{PDGF} offers a PDGF-BB concentration-dependent detection signal, and the mCherry signal in the localization module worked as a reference signal. As expected, the FAM signal of **CPNN$_{PDGF}$** gradually increased in the presence of PDGF-BB, whereas the fluorescence intensity of mCherry remained stable (Fig. S14B and C†). Additionally, similar trends were observed in the measurements of relative fluorescence quantum yields of FAM and mCherry in the S_{PDGF} (Table S5†). Meanwhile, the ratiometric signal $F_{FAM}/F_{mCherry}$ increased linearly with the concentration of PDGF-BB ranging from 0.2 to 10 nM, with a detection limit as low as 0.06 nM. Despite achieving a comparable linear range and detection limit, the ratiometric **CPNN$_{PDGF}$** exhibits enhanced reliability attributed to its self-calibration capability. Further, we assessed the photostability of the proposed **CPNN$_{PDGF}$** following its incubation with PDGF-BB. As shown in Fig. S15,† the fluorescence intensity of FAM in **CPNN$_{PDGF}$** remained relatively stable even after 1 hour and exhibited a decrease of 30% after 3 hours of irradiation, while the fluorescence intensity of mCherry remained almost unchanged. Notably, enhanced photostability of **CPNN** can be achieved by adopting more durable fluorescent dyes, such as Cy5. Together, these results demonstrate the high potential of **CPNN$_{PDGF}$** for detecting PDGF-BB in complex environments.

CPNN$_{PDGF}$-based PDGF-BB imaging in the collagen-coated plates

Before *in situ* monitoring of PDGF-BB in the TME, we first evaluated the response of **CPNN$_{PDGF}$** to PDGF-BB in the collagen-coated 96-microwell plate by fluorescence imaging, utilizing a Cy5-labeled S_{PDGF} (Fig. 3A). Fig. 3B and C depict that, after treatment of **CPNN$_{PDGF}$**, the collagen-coated wells exhibited bright mCherry fluorescence signals, indicating the efficient binding of **CPNN$_{PDGF}$** to collagen. Further incubation with PDGF-BB resulted in a significant increase in the Cy5 signal, which colocalized well with the mCherry signal. The ratiometric signal ($F_{Cy5}/F_{mCherry}$) was calculated as approximately 1.27 by dividing the fluorescence intensity of Cy5 by that of mCherry (Fig. 3D). In comparison, although the control group **mCPNN$_{PDGF}$** (constructed by coupling CmD and mS_{PDGF}) can immobilize the collagen-coated wells, there was no obvious Cy5 fluorescence signal upon the addition of PDGF, indicating the critical role of the aptamer-mediated target recognition in the nanodevice (Fig. S16†).

Next, the ability of **CPNN$_{PDGF}$** for semiquantitative analysis of PDGF-BB at the interface was evaluated. The collagen-coated wells were pretreated with **CPNN$_{PDGF}$**, followed by washing and subsequent incubation with PBS-HSA buffers containing different concentrations of PDGF-BB. As shown in Fig. 3E and F, the fluorescence signal of Cy5 gradually increased with the increasing concentration of adscititious PDGF-BB, while the signal of mCherry remained relatively stable. The ratiometric signal $F_{Cy5}/F_{mCherry}$ was calculated using ImageJ software and showed a concentration-dependent pattern in response to PDGF-BB concentration ranging from 0 to 200 nM. Moreover, the collagen-coated well treated with 200 nM of PDGF-BB exhibited a ratiometric signal approximately 10-fold higher

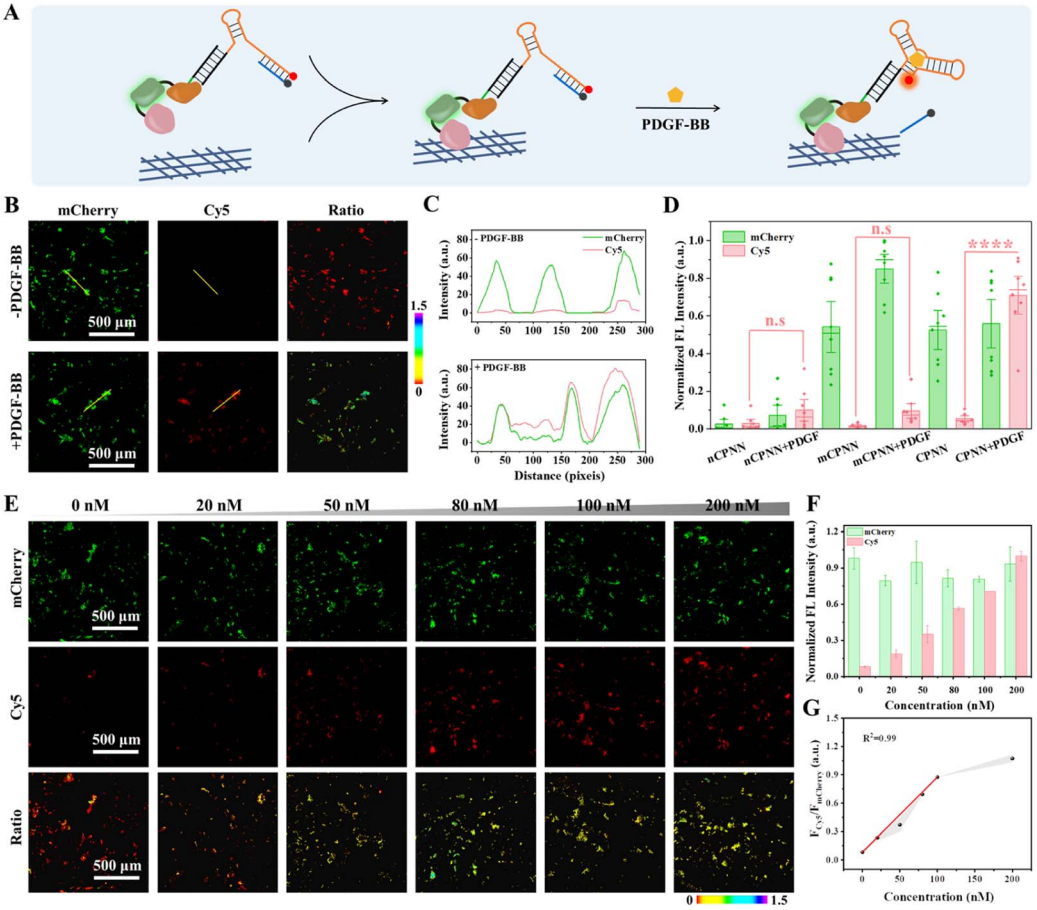

Fig. 3 $CPNN_{PDGF}$-based fluorescence imaging of PDGF-BB on the interface of the collagen-coated wells. (A) Schematic illustration of $CPNN_{PDGF}$ in response to PDGF-BB in a 96-microwell plate. (B) Fluorescence imaging of the collagen-coated wells pretreated with $CPNN_{PDGF}$ in the presence and absence of PDGF-BB, respectively. (C) Intensity profiles of mCherry and Cy5 along the yellow arrow in the wells in panel (B). (D) Quantitative analysis of fluorescence intensities of the collagen-coated wells treated with $nCPNN_{PDGF}$, $mCPNN_{PDGF}$, and $CPNN_{PDGF}$ in the presence or absence of PDGF-BB. (E) Fluorescence images and the corresponding ratiometric images of $CPNN_{PDGF}$ in response to different concentrations of PDGF-BB. (F) Quantitative analysis of the intensities of mCherry and Cy5 and (G) $F_{Cy5}/F_{mCherry}$ as a function of PDGF-BB concentration derived from the corresponding images in (E). Collagen III, 10 μg mL; $CPNN_{PDGF}$, 200 nM. mCherry: E_x 555 nm/E_m 610 nm; Cy5: E_x 635 nm/E_m 670 nm. Scale bar, 500 μm.

than that of the untreated collagen-coated well (Fig. 3G). Therefore, the CBD-based collagen binding did not affect the PDGF-BB sensing capacity of $CPNN_{PDGF}$. The ratiometric signal with an excellent signal-to-noise ratio indicated both the reliability and sensitivity of $CPNN_{PDGF}$ for the detection of PDGF-BB at the interface. In combination, $CPNN_{PDGF}$ exhibited a satisfactory imaging capability and allowed semi-quantitative detection of PDGF-BB after immobilization with collagen.

Expression and binding of collagen in the tumor spheroids

Encouraged by the fluorescence imaging outcomes on the collagen-coated plates, we wanted to know whether **CPNN** can immobilize the TME through collagen binding. Three-dimensional (3D) multicellular tumor spheroid models serve as an intermedia model bridging the gap between *in vitro* and *in vivo* systems and have attracted considerable interest from the scientific community.[49] Rather than the traditional 2D culture system, tumor spheroids, which contain the complex and dynamic intercellular communication and cell–matrix interactions inherent to cancer metastasis, more closely mimic the TME of tumor growth and progression, providing a comprehensive understanding of the fundamental characteristics of tumor tissues and the complexities of cancer metastasis.[50–52] Therefore, using tumor spheroids as a model provides an opportunity for *in situ* imaging of cancer biomarkers within the TME and a deep understanding of the biological mechanisms of these cancer biomarkers in cancer progression.

Before **CPNN** binding, the presence of collagen in the TME of MCF-7 (a breast cancer cell) tumor spheroids was investigated through immunofluorescence staining. Fig. S17† demonstrates that after the MCF-7 tumor spheroid was treated with the rabbit anti-collagen antibody and the Alex Fluor 594 labeled goat anti-rabbit IgG, there was obvious red fluorescence around the spheroids. It is consistent with the literature that abundant collagen is present in the TME of tumor spheroids.[53,54] When the tumor spheroids were mixed with the fusion proteins, only

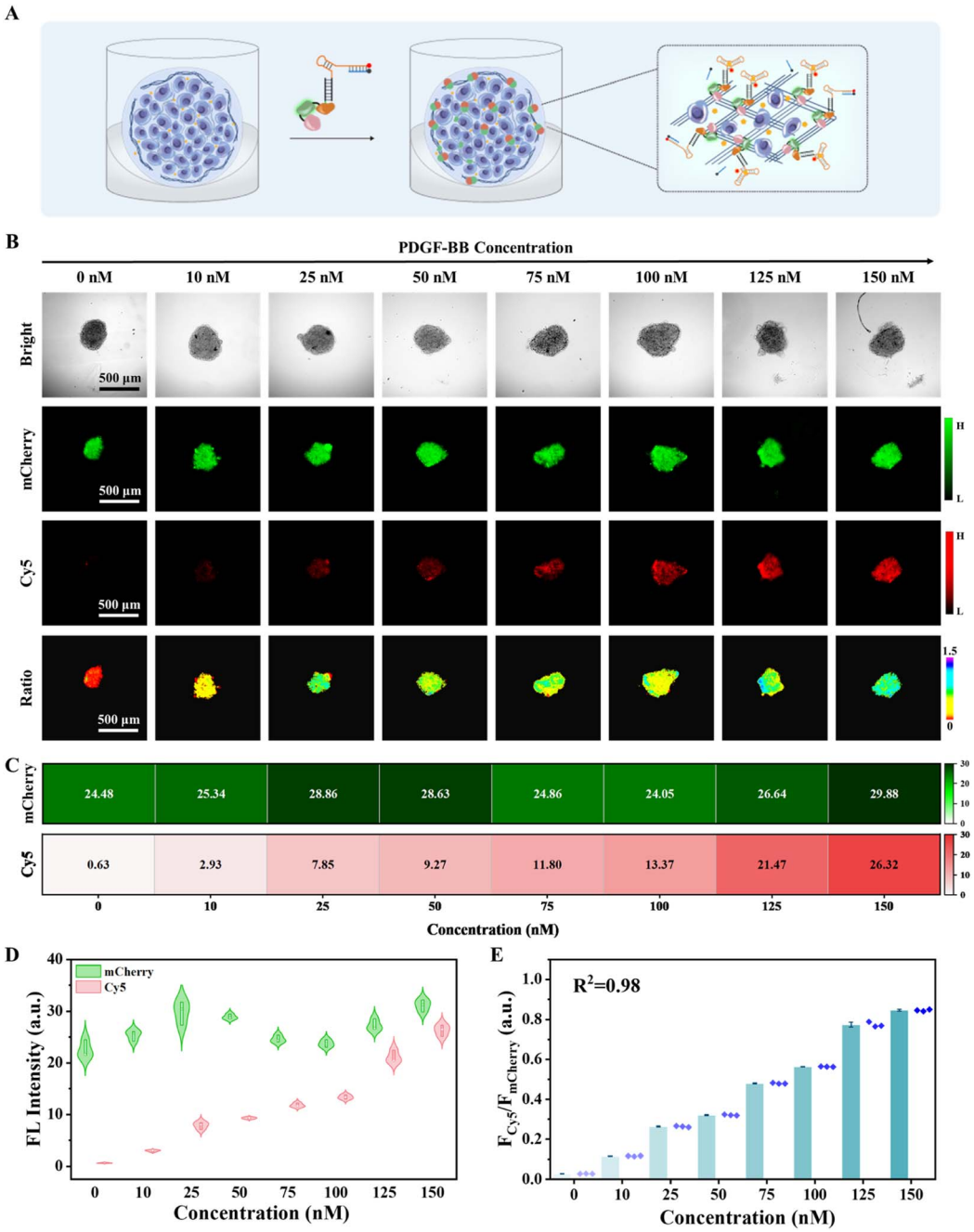

Fig. 4 *In situ* ratiometric fluorescence imaging of PDGF-BB in the MCF-7 tumor spheroids using **CPNN**$_{PDGF}$. (A) Schematic illustration of **CPNN**$_{PDGF}$ responding to PDGF-BB in the tumor spheroids. (B) Fluorescence images and corresponding ratiometric images of the tumor spheroids pre-treated with **CPNN**$_{PDGF}$ in response to different concentrations of PDGF-BB. (C) Heat map indicating the fluorescence signal of the tumor spheroids pre-treated with **CPNN**$_{PDGF}$ incubated with different concentrations of PDGF-BB. (D) The intensities of mCherry and Cy5, as well as (E) $F_{Cy5}/F_{mCherry}$ signal as a function of PDGF-BB concentration, derived from corresponding images in (B). mCherry: E_x 555 nm/E_m 610 nm; Cy5: E_x 635 nm/E_m 670 nm. Scale bar, 500 μm.

those incubated with the fusion protein containing CBD (CmD) showed a prominent mCherry signal. Furthermore, the tumor spheroids incubated with CmD-ssDNA$_{DCV}$-Cy5 exhibited the mCherry and Cy5 signals with a high PC of 0.97 (Fig. S18†). This correlation suggests the effective coupling of DCV to nucleic acid and the efficient immobilization of the fusion protein and the nanodevice on the tumor spheroids through collagen binding, providing a robust basis for **CPNN**-based detection of the biomarker in the TME.

CPNN$_{PDGF}$-based PDGF-BB imaging in the TME of tumor spheroids

The TME is a highly intricate physical and biochemical system that comprises a multitude of cancer biomarkers intimately

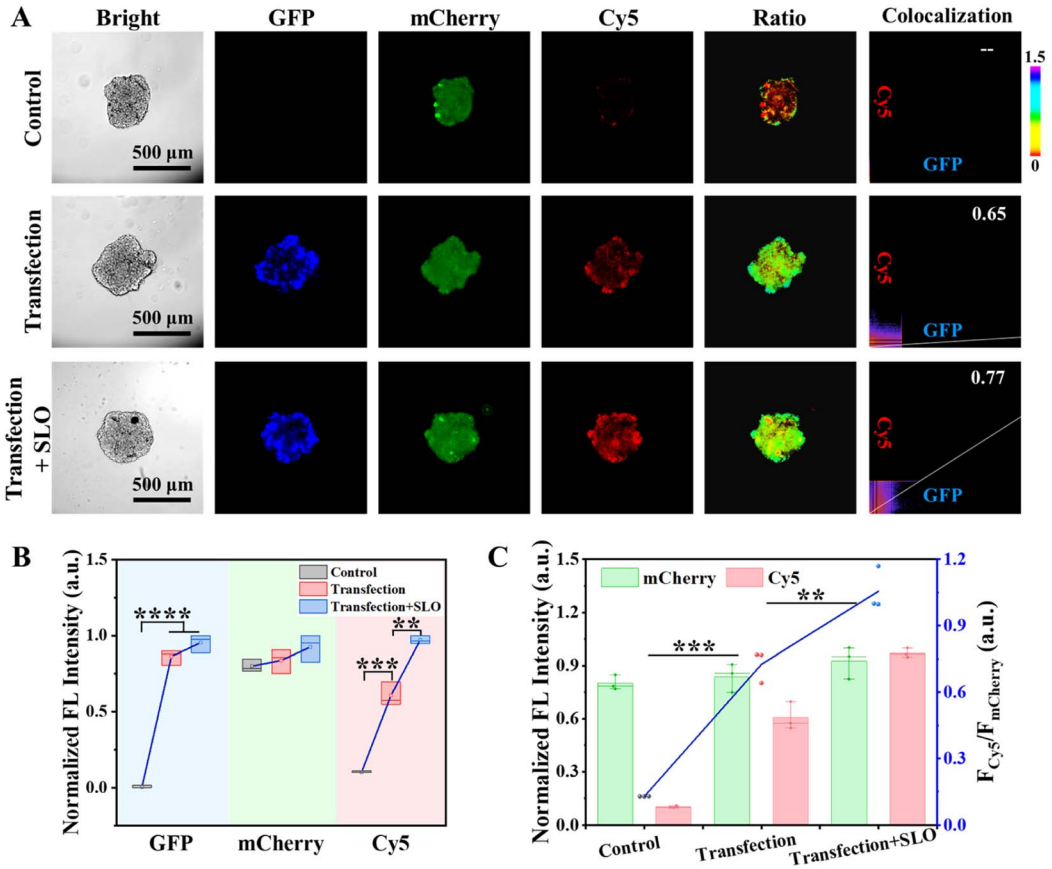

Fig. 5 $CPNN_{PDGF}$-based *in situ* imaging of PDGF-BB secretion and release by the MCF-7 tumor spheroids. (A) Representative fluorescence images of the tumor spheroids under different conditions. (B) Normalized fluorescence intensity of the GFP, mCherry, and Cy5 channels, and (C) quantification of the ratiometric signal $F_{Cy5}/F_{mCherry}$ from the tumor spheroids. GFP: E_x 485 nm/E_m 520 nm; mCherry: E_x 555 nm/E_m 610 nm; Cy5: E_x 635 nm/E_m 670 nm. Scale bar, 500 μm.

linked to tumor growth, invasion, and metastasis.[3,4] Based on the promising fluorescence imaging results obtained in collagen-coated microplates and efficient immobilization of the chimeric protein-nucleic acid in the tumor spheroids, we investigated the sensing capability of $\mathbf{CPNN_{PDGF}}$ in the complex TME of MCF-7 tumor spheroids. First, the biocompatibility of the fusion protein CmD and the nanodevice $\mathbf{CPNN_{PDGF}}$ was assessed using the CCK-8 method. It was found that incubation with different concentrations of CmD and $\mathbf{CPNN_{PDGF}}$ for different durations did not obviously change the viability of MCF-7 cells under the experimental conditions (Fig. S19 and S20†). Encouraged by favourable biocompatibility, we then evaluated the feasibility of $\mathbf{CPNN_{PDGF}}$ for sensing and imaging PDGF-BB in MCF-7 tumor spheroids (Fig. 4A). The tumor spheroids incubated with $\mathbf{CPNN_{PDGF}}$ emitted a clear mCherry signal. The addition of PDGF-BB largely increased the signal from the Cy5 channel, which colocalized well with the mCherry signal. Ratiometric fluorescence imaging and $F_{Cy5}/F_{mCherry}$ analysis further confirmed that the tumor spheroids pretreated with $\mathbf{CPNN_{PDGF}}$ exhibited a clear ratiometric fluorescence signal upon exposure to PDGF-BB, resulting in a significant increase in $F_{Cy5}/F_{mCherry}$ values from 0.03 to 1.21 (Fig. S21†). In contrast, the Cy5 fluorescence signal of the tumor spheroids in the $\mathbf{mCPNN_{PDGF}}$ group was negligible due to the low affinity between mS_{PDGF} and PDGF-BB. These results collectively indicate that $\mathbf{CPNN_{PDGF}}$ anchored to the tumor spheroids retains its ability to respond to PDGF-BB.

Further, the analytical performance of $\mathbf{CPNN_{PDGF}}$ for PDGF-BB sensing and imaging in tumor spheroids was assessed. The tumor spheroids pre-treated with $\mathbf{CPNN_{PDGF}}$ were incubated with different concentrations of PDGF-BB, and imaging was performed after 1 hour of incubation (Fig. 4B). Consistent with the findings at the interface of the 96-microwell plate, as the concentrations of PDGF-BB gradually increased from 0 to 150 nM, the fluorescence intensity of mCherry on the tumor spheroids remained relatively stable, whereas the fluorescence intensity of Cy5 exhibited a significant increase (Fig. 4C). However, as shown by the change in the mCherry signal, the signal fluctuation among the tumor spheroids was obvious, and the linear relationship between the Cy5 signal and the PDGF-BB concentration was not particularly good ($R^2 = 0.95$) (Fig. 4D and S22†). Conversely, using mCherry as a reference signal, the ratiometric signal $F_{Cy5}/F_{mCherry}$ exhibited a better concentration-dependent increase ($R^2 = 0.98$) within the PDGF-BB concentration range of 0–150 nM. The detection limit for PDGF-BB in tumor spheroids was determined to be 0.16 nM based on the

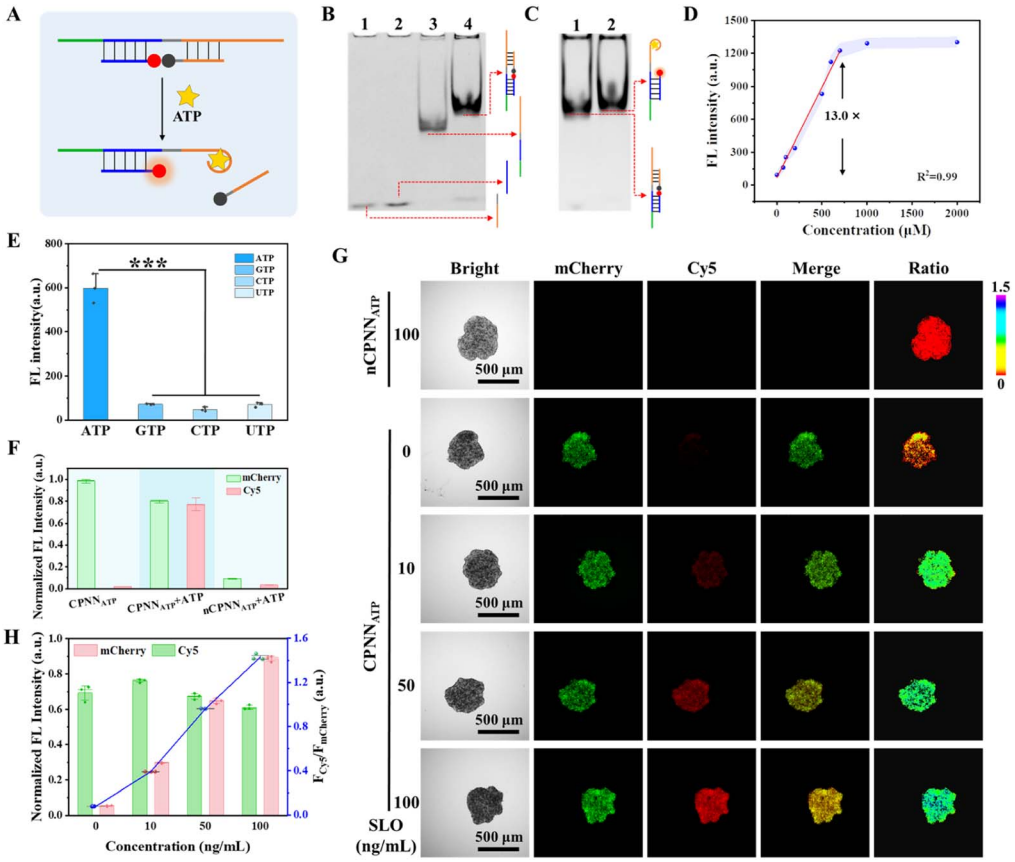

Fig. 6 $CPNN_{ATP}$-based *in situ* ATP detection. (A) Schematic illustration of the design of S_{ATP} and its response to ATP. (B) Native PAGE analysis of S_{ATP} assembly and (C) in the presence of ATP. (D) Calibration curve of the fluorescence intensity as a function of the ATP concentration. (E) The fluorescence signal of $CPNN_{ATP}$ in response to ATP and other nucleoside triphosphates. Each nucleoside triphosphate concentration is 500 μM. (F) Representative fluorescence intensities of the tumor spheroids treated with $CPNN_{ATP}$ and $nCPNN_{ATP}$ in the presence or absence of ATP, respectively. (G) Fluorescence images and the corresponding ratiometric fluorescence images of the $CPNN_{ATP}$-treated tumor spheroids with different concentrations of SLO. (H) Normalized fluorescence intensity of the mCherry and Cy5 channels and quantification of the ratiometric signal $F_{Cy5}/F_{mCherry}$ on the tumor spheroids. mCherry: E_x 555 nm/E_m 610 nm; Cy5: E_x 635 nm/E_m 670 nm. Scale bar, 500 μm.

quantitative results obtained through fluorescence imaging (3σ/slope, Fig. 4E), which was slightly higher than the detection limit in solution (0.06 nM). Notably, the extracellular concentration of PDGF-BB in the TME often exceeds those in serum (0.4–0.7 nM under physiological conditions and higher under pathological conditions) due to enrichment in the local microenvironment, and falls well within the detectable range of the proposed $CPNN_{PDGF}$.[47,48] The self-calibration capability of the fluorescence signals improved the accuracy of the proposed method. Therefore, the nanodevice $CPNN_{PDGF}$ has the potential to be an effective tool for *in situ* semi-quantitative imaging of PDGF-BB in tumor spheroids.

Given the pivotal role of PDGF-BB in the progression of numerous solid tumors, endogenous PDGF-BB in the TME was monitored using $CPNN_{PDGF}$. To mimic the endogenic production and release of PDGF-BB, a construct pCMV3-*pdgf-gfp* containing the fusion gene of the GFP-tagged human PDGF-BB was transiently transfected into the cells, and the tumor spheroids using Lipofectamine™ 8000 transfection reagent, respectively. It was found that both the 2D cultured MCF-7 cells and the 3D tumor spheroids emitted bright green fluorescence, which indicated the successful expression of PDGF-BB in the cells (Fig. S23†). We then used $CPNN_{PDGF}$ to monitor the endogenic PDGF-BB within the tumor spheroids. Streptolysin O (SLO), a member of cytolysins that can bind to eukaryotic cells and promote cytolysis by forming transmembrane pores, was used to release PDGF-BB. At this time, we utilized the "always on" fluorescence of mCherry to track the anchoring of $CPNN_{PDGF}$ on tumor spheroids, the "always on" fluorescence of GFP to label the expression and localization of PDGF-BB, and the "activated" fluorescence of Cy5 to monitor the secretion and release of PDGF-BB. As expected, the fluorescence signals of mCherry were detected in all groups, and only the transfection groups exhibited GFP signals (Fig. 5A and B). While a weak Cy5 signal was detected around the un-transfected tumor spheroids, a significant increase of the Cy5 signal with an $F_{Cy5}/F_{mCherry}$ of 0.73 was observed in the transfected group (Fig. 5), which was comparable to that of the 125 nM PDGF-BB-treated group in Fig. 4E. Considering that $CPNN_{PDGF}$ was anchored on collagen in the TME, this bright Cy5 signal suggested that PDGF-BB was released from the cells, just like other cytokines. Furthermore, the fluorescence of Cy5 was enhanced by approximately 1.6

times following SLO treatment with an $F_{Cy5}/F_{mCherry}$ of 1.06 (Fig. 5), suggesting that the addition of SLO potentially facilitated the release of PDGF-BB by inducing cell membrane perforation, which was consistent with the literature.[17] Notably, the Cy5 signal of **CPNN**$_{PDGF}$ exhibited excellent overlap not only with the mCherry signal but also with the GFP signal of the secreted PDGF-BB (PC > 0.65), indicating the ability of our method to monitor both the expression level and localization of PDGF-BB (Fig. 5A). These results suggested that **CPNN**$_{PDGF}$ could successfully monitor PDGF-BB levels in tumor spheroids, indicating its potential as a valuable tool for cancer diagnosis and evaluation of therapeutic approaches.

Expanding the strategy for *in situ* imaging of ATP in the TME

As a modularized nanodevice, **CPNN** has the potential to detect other targets *in situ* by simply changing the aptamer of the sensing module. Given its pivotal role in cellular metabolism and regulation, ATP, as a typical cancer biomarker, was selected as another target to evaluate the expandability of **CPNN**.[55,56] We first designed a sensing module specifically responsive to ATP (S_{ATP}, Fig. 6A and S24†). The assembly of S_{ATP} and its ability to bind ATP were confirmed by PAGE analysis (Fig. 6B and C), and its feasibility for ATP detection was further demonstrated by fluorescence spectrum measurements. As shown in Fig. S25† and 6D, the fluorescence signal of Cy5 exhibited a linear correlation with the ATP concentration, and the calibration curve for the ATP assay shows linearity in the concentration range of 50–700 μM, with a detection limit of 10 μM (3σ/slope). Due to the high specificity of the aptamer for the target, this S_{ATP} exhibited unique selectivity for ATP (Fig. 6E and S26†). After confirming the high biocompatibility of **CPNN**$_{ATP}$ under the experimental conditions (Fig. S27†), the feasibility of **CPNN**$_{ATP}$ for sensing and imaging ATP in the tumor spheroids was assessed through fluorescence imaging. As depicted in Fig. 6F, a strong Cy5 signal from the immobilized **CPNN**$_{ATP}$ was detected within the tumor spheroids in the presence of ATP. Endogenous ATP released during cellular necrosis was further detected. Here, the tumor spheroids anchored with **CPNN**$_{ATP}$ were treated with different concentrations of SLO for 1 hour before fluorescence imaging. As expected, the fluorescence signal of Cy5 and the resulting ratiometric signal $F_{Cy5}/F_{mCherry}$ increased sensitively with the increasing SLO concentration (Fig. 6F–H). In contrast, the control **nCPNN**$_{ATP}$ (mD-S$_{ATP}$) showed a weak fluorescent signal even in the presence of high concentrations of SLO due to the absence of the CBD anchor unit. Together, these data demonstrate the promising performance of **CPNN**$_{ATP}$ for *in situ* imaging of ATP in the tumor spheroids and present the flexible design of this chimeric protein-nucleic acid nanodevice for *in situ* detection of different targets.

Conclusions

In summary, we designed a versatile chimeric protein–nucleic acid nanodevice (**CPNN**) consisting of a multifunctional fusion protein CmD and an aptamer-based sensing module. **CPNN** can be specifically anchored on collagen, enabling sensitive and accurate *in situ* ratiometric imaging of exogenous and endogenous PDGF-BB in the tumor spheroids. Notably, we also validated the efficacy of this approach for spatiotemporal imaging of ATP in the tumor spheroids by substituting the sensing module with an ATP-responsive one. To our knowledge, this is the first example of a collagen-binding chimeric protein-nucleic acid reporter for ratiometric imaging of cancer biomarkers in the TME.

CPNN in this study offers several advantages: (i) DCV-based efficient coupling between the sensing module and the protein module endows **CPNN** with the dual advantages of both protein and nucleic acid; (ii) it uses the high affinity of CBD for collagen to achieve specific and stable *in situ* anchoring, enabling the co-localization of the nanodevice for intuitive and precise visualization and monitoring of critical information in the TME; (iii) the design of the aptamer-based sensing module makes it possible to expand the range to various biomarkers; (iv) the ratiometric fluorescence design results in improved accuracy. We believe that this straightforward yet potent approach offers a versatile imaging platform capable of elucidating the biological functions of cancer biomarkers in the TME and being valuable for early cancer diagnosis and therapeutic applications.

Data availability

All data required to evaluate the conclusions are present in the paper and/or ESI.†

Author contributions

F. Tian, Y. Huang, and Z. Nie proposed the idea, designed the experiments, and revised the manuscript. F. Tian performed experimental work and wrote the manuscript. S. Zhou, S. Xie, and Z. Zhang performed most assays. L. Peng, L. Jiang, and Z. Wang assisted in plasmid construction, protein expression, and purification. All authors contributed to the manuscript.

Conflicts of interest

The author(s) declare that they have no competing interests.

Acknowledgements

This work was supported by the National Key R&D Program of China (2021YFA0910100), the National Natural Science Foundation of China (22074034, 22034002, 22274041, and 22204047), and the Fundamental Research Funds for the Central Universities.

Notes and references

1 D. F. Quail and J. A. Joyce, *Nat. Med.*, 2013, **19**, 1423–1437.
2 S. Sanegre, F. Lucantoni, R. Burgos-Panadero, L. de La Cruz-Merino, R. Noguera and T. Álvaro Naranjo, *Cancers*, 2020, **12**, 1677.

3 S. Wang, W. X. Ren, J. T. Hou, M. Won, J. An, X. Y. Chen, J. Shu and J. S. Kim, *Chem. Soc. Rev.*, 2021, **50**, 8887–8902.
4 X. Li, P. Ramadori, D. Pfister, M. Seehawer, L. Zender and M. Heikenwalder, *Nat. Rev. Cancer*, 2021, **21**, 541–557.
5 M. Gullberg, S. M. Gústafsdóttir, E. Schallmeiner, J. Jarvius, M. Bjarnegård, C. Betsholtz, U. Landegren and S. Fredriksson, *Proc. Natl. Acad. Sci. U. S. A.*, 2004, **101**, 8420–8424.
6 N. Cohen, P. Sabhachandani, A. Golberg and T. Konry, *Biosens. Bioelectron.*, 2015, **66**, 454–460.
7 H. M. Da, H. Y. Liu, Y. N. Zheng, R. Yuan and Y. C. Chai, *Biosens. Bioelectron.*, 2018, **101**, 213–218.
8 C. M. Cao, F. Y. Zhang, E. M. Goldys, F. Gao and G. Z. Liu, Advances in structure-switching aptasensing towards real time detection of cytokines, *TrAC, Trends Anal. Chem.*, 2018, **102**, 379–396.
9 A. L. Chen, M. M. Yan and S. M. Yang, *TrAC, Trends Anal. Chem.*, 2016, **80**, 581–593.
10 H. R. Jia, Y. X. Zhu, Q. Y. Duan and F. G. Wu, *Chem. Soc. Rev.*, 2021, **50**, 6240–6277.
11 S. Shi, J. Chen, X. W. Wang, M. S. Xiao, A. R. Chandrasekaran, L. Li, C. Q. Yi and H. Pei, *Adv. Funct. Mater.*, 2022, **32**, 2201069.
12 L. L. Chen, Y. F. Lyu, X. Zhang, L. T. Zheng, Q. Q. Li, D. Ding, F. M. Chen, Y. H. Liu, W. Li, Y. T. Zhang, Q. L. Huang, Z. Q. Wang, T. T. Xie, Q. Zhang, Y. Y. Sima, K. Li, S. Xu, T. B. Ren, M. Y. Xiong, Y. Wu, J. B. Song, L. Yuan, H. H. Yang, X. B. Zhang and W. H. Tan, *Sci. China: Chem.*, 2023, **66**, 1336–1383.
13 Y. X. Zhao, X. L. Zuo, Q. Li, F. Chen, Y. R. Chen, J. Q. Deng, D. Han, C. L. Hao, F. J. Huang, Y. Y. Huang, G. L. Ke, H. Kuang, F. Li, J. Li, M. Li, N. Li, Z. Y. Lin, D. B. Liu, J. W. Liu, L. B. Liu, X. G. Liu, C. H. Lu, F. Luo, X. H. Mao, J. S. Sun, B. Tang, F. Wang, J. B. Wang, L. H. Wang, S. Wang, L. L. Wu, Z. S. Wu, F. Xia, C. L. Xu, Y. Yang, B. F. Yuan, Q. Yuan, C. Zhang, Z. Zhu, C. Y. Yang, X. B. Zhang, H. H. Yang, W. H. Tan and C. H. Fan, *Sci. China: Chem.*, 2021, **64**, 171–203.
14 L. Li, Y. Jiang, C. Cui, Y. Yang, P. H. Zhang, K. Stewart, X. S. Pan, X. W. Li, L. Yang, L. P. Qiu and W. H. Tan, *J. Am. Chem. Soc.*, 2018, **140**, 13335–13339.
15 Y. Zhou, Y. Zhuo, R. Peng, Y. Zhang, Y. Du, Q. Zhang, Y. Sun and L. Qiu, *Sci. China: Chem.*, 2021, **64**, 1817–1825.
16 L. P. Qiu, T. Zhang, J. H. Jiang, C. C. Wu, G. Z. Zhu, M. X. You, X. G. Chen, L. Q. Zhang, C. Cui, R. Q. Yu and W. H. Tan, *J. Am. Chem. Soc.*, 2014, **136**, 13090–13093.
17 Z. H. Di, J. Zhao, H. Q. Chu, W. T. Xue, Y. L. Zhao and L. L. Li, *Adv. Mater.*, 2019, **31**, 1901885.
18 G. F. Feng, X. Y. Luo, X. Lu, S. Y. Xie, L. Deng, W. Y. Kang, F. He, J. H. Zhang, C. Y. Lei, B. Lin, Y. Huang, Z. Nie and S. Z. Yao, *Angew. Chem., Int. Ed.*, 2019, **58**, 6590–6594.
19 X. M. Dong, L. X. Sun, Z. W. Zhang, T. L. Zhu, J. Sun, J. Z. Gao, C. J. Dong, R. C. Wang, X. F. Gu and C. C. Zhao, *Sci. China: Chem.*, 2023, **66**, 1869–1876.
20 J. Y. Shi, C. Clayton and B. Z. Tian, *Nano Res.*, 2019, **13**, 1214–1227.
21 Z. D Wu, M. S. Xiao, W. Lai, Y. Y. Sun, L. Li, Z. Q. Hu and H. Pei, *ACS Appl. Bio Mater.*, 2022, **5**, 1901–1915.
22 W. A. Zhao, S. Schafer, J. Choi, Y. J. Yamanaka, M. L. Lombardi, S. Bose, A. L. Carlson, J. A. Phillips, W. Teo, I. A. Droujinine, C. H. Cui, R. K. Jain, J. Lammerding, J. C. Love, C. P. Lin, D. Sarkar, R. Karnik and J. M. Karp, *Nat. Nanotechnol.*, 2011, **6**, 524–531.
23 L. P. Qiu, F. Wimmers, J. Weiden, H. A. Heus, J. Tel and C. G. Figdor, *Chem. Commun.*, 2017, **53**, 8066–8069.
24 D. D. Chao, X. M. Xu, Y. Y. Miao, L. L. Yang, Q. Q. Gao, R. Xu, Y. Tian, Y. M. Zhao, Y. M. Du and D. Han, *Sci. China: Chem.*, 2022, **65**, 2327–2334.
25 X. L. Huang, J. B. Song, B. C. Yung, X. H. Huang, Y. H. Xiong and X. Y. Chen, *Chem. Soc. Rev.*, 2018, **47**, 2873–2920.
26 Y. Z. Shen, Y. L. Wei, C. L. Zhu, J. X. Cao and D. M. Han, *Coord. Chem. Rev.*, 2022, **458**, 214442.
27 S. P. Zhang, H. Chen, L. P. Wang, X. Qin, B. P. Jiang, S. C. Ji, X. C. Shen and H. Liang, *Angew. Chem., Int. Ed.*, 2022, **61**, e202107076.
28 G. Grasso, F. Colella, S. Forciniti, V. Onesto, H. Iuele, A. C. Siciliano, F. Carnevali, A. Chandra, G. Gigli and L. L. del Mercato, *Nanoscale Adv.*, 2023, **5**, 4311–4336.
29 X. Li and J. W. Dai, *Biomater. Sci.*, 2018, **6**, 265–271.
30 X. Z. Liu, L. L. Zhang, Z. J. Xu, X. Xiong, Y. Z. Yu, H. F. Wu, H. Qiao, J. J. Zhong, Z. Zhao, J. W. Dai and G. L. Suo, *Acta Biomater.*, 2022, **154**, 385–400.
31 J. Adams and R. W. Farndale, *Essays Biochem.*, 2019, **63**, 337–348.
32 J. K. Mouw, G. Q. Ou and V. M. Weaver, *Nat. Rev. Mol. Cell Biol.*, 2014, **15**, 771–785.
33 K. Sasaki, J. Ishihara, A. Ishihara, R. Miura, A. Mansurov, K. Fukunaga and J. A. Hubbell, *Sci. Adv.*, 2019, **5**, eaaw6081.
34 J. Ishihara, A. Ishihara, K. Sasaki, S. S. Y. Lee, J. M. Williford, M. Yasui, H. Abe, L. Potin, P. Hosseinchi, K. Fukunaga, M. M. Raczy, L. T. Gray, A. Mansurov, K. Katsumata, M. Fukayama, S. J. Kron, M. A. Swartz and J. A. Hubbell, *Sci. Transl. Med.*, 2019, **11**, eaau3259.
35 A. Mansurov, J. Ishihara, P. Hosseinchi, L. Potin, T. M. Marchell, A. Ishihara, J. M. Williford, A. T. Alpar, M. M. Raczy, L. T. Gray, M. A. Swartz and J. A. Hubbell, *Nat. Biomed. Eng.*, 2020, **4**, 531–543.
36 K. N. Lovendahl, A. N. Hayward and W. R. Gordon, *J. Am. Chem. Soc.*, 2017, **139**, 7030–7035.
37 S. F. Hu, J. H. Zhang, R. Tang, J. H. Fan, H. Q. Liu, W. Y. Kang, C. Y. Lei, Z. Nie, Y. Huang and S. Z. Yao, *Anal. Chem.*, 2019, **91**, 10180–10187.
38 K. Hosaka, Y. L. Yang, T. Seki, C. Fischer, O. Dubey, E. Fredlund, J. Hartman, P. Religa, H. Morikawa, Y. Ishii, M. Sasahara, O. Larsson, G. Cossu, R. H. Cao, S. Lim and Y. H. Cao, *Proc. Natl. Acad. Sci. U. S. A.*, 2016, **113**, 5618–5627.
39 C. Q. Vu, P. Rotkrua and Y. Tantirungrotechai, *ACS Comb. Sci.*, 2017, **19**, 609–617.
40 Z. Y. Xia, Y. Xing, J. Jeon, Y. P. Kim, J. Gall, A. Dragulescu-Andrasi, S. S. Gambhir and J. H. Rao, *ACS Chem. Biol.*, 2011, **6**, 1117–1126.

41 R. Tang, Y. H. Fu, B. Gong, Y. Y. Fan, H. H. Wang, Y. Huang, Z. Nie and P. Wei, *Angew. Chem., Int. Ed.*, 2022, **61**, e202205902.
42 P. Romero, A. Donda and J. A. Hubbell, *Nat. Biomed. Eng.*, 2020, **4**, 583–584.
43 M. J. Wang, Y. F. Da and Y. Tian, *Chem. Soc. Rev.*, 2023, **52**, 1189–1214.
44 M. Tsioumpekou, S. I. Cunha, H. S. Ma, A. Åhgren, J. Cedervall, A. K. Olsson, C. H. Heldin and J. Lennartsson, *Theranostics*, 2020, **10**, 1122–1135.
45 M. Kirsch, J. C. Wilson and B. Peter, *J. Neuro-Oncol.*, 1997, **35**, 289–301.
46 A. Csordas, A. E. Gerdon, J. D. Adams, J. R. Qian, S. S. Oh, Y. Xiao and H. T. Soh, *Angew. Chem., Int. Ed.*, 2010, **49**, 355–358.
47 D. A. Bronzert, P. Pantazis, H. N. Antoniades, A. Kasid, N. Davidson, R. B. Dickson and M. E. Lippman, *Proc. Natl. Acad. Sci. U. S. A.*, 1987, **84**, 5763–5767.
48 S. Fredriksson, M. Gullberg, J. Jarvius, C. Olsson, K. Pietras, S. M. Gústafsdóttir, A. Östman and U. Landegren, *Nat. Biotechnol.*, 2002, **20**, 473–477.
49 S. J. Han, S. Kwon and K. S. Kim, *Cancer Cell Int.*, 2021, **21**, 152.
50 F. Pampaloni, E. G. Reynaud and E. H. K. Stelzer, *Nat. Rev. Mol. Cell Biol.*, 2007, **8**, 839–845.
51 X. Xu, M. C. Farach-Carson and X. Q. Jia, *Biotechnol. Adv.*, 2014, **32**, 1256–1268.
52 B. Pinto, A. C. Henriques, P. M. A. Silva and H. Bousbaa, *Pharmaceutics*, 2020, **12**, 1186.
53 J. Winkler, A. Abisoye-Ogunniyan, K. J. Metcalf and Z. Werb, *Nat. Commun.*, 2020, **11**, 5120.
54 A. D. Theocharis, S. S. Skandalis, C. Gialeli and N. K. Karamanos, *Adv. Drug Delivery Rev.*, 2016, **97**, 4–27.
55 S. Y. Chen, R. J. Wang, S. Peng, S. Y. Xie, C. Y. Lei, Y. Huang and Z. Nie, *Chem. Sci.*, 2022, **13**, 2011–2020.
56 F. Di Virgilio, A. C. Sarti, S. Falzoni, E. De Marchi and E. Adinolfi, *Nat. Rev. Cancer*, 2018, **18**, 601–618.